Inducing in operando chloride ion filtration through an electrocatalytic film architecture integrated with ZIF-8 nanosheets En route to seawater electrolysis

Catherine Harvey, Simon Delacroix, Clément Marchat, Thierry Gacoin, Cédric Tard

Electrochimica Acta 544 (2025) 147664

Contents lists available at ScienceDirect

Electrochimica Acta

journal homepage: www.journals.elsevier.com/electrochimica-acta

Inducing *in operando* chloride ion filtration through an electrocatalytic film architecture integrated with ZIF-8 nanosheets En route to seawater electrolysis

Catherine Harvey [a,b,1], Simon Delacroix [b], Clément Marchat [b], Thierry Gacoin [b], Cédric Tard [a,*]

[a] Laboratoire de Chimie Moléculaire (LCM), CNRS, École Polytechnique, Institut Polytechnique de Paris, 91120 Palaiseau, France
[b] Laboratoire de Physique de la Matière Condensée (PMC), CNRS, École Polytechnique, Institut Polytechnique de Paris, 91120 Palaiseau, France

ARTICLE INFO

Keywords:
Electrolysis
Seawater
Oxygen evolution reaction
Chlorine evolution reaction
ZIF-8 nanosheets
In-Situ Filtration

ABSTRACT

Ameliorating direct seawater electrolysis to produce green hydrogen requires an advancement in the conception of material designs and electrocatalytic film architectures. Indeed, to complement the hydrogen evolution reaction (HER) at the cathode, oxygen must be produced thanks to the oxygen evolution reaction (OER) at the anode. Nevertheless, this kinetically slow reaction is in competition with the kinetically facile chlorine evolution reaction (CER). In this work, the entropic selectivity of the ZIF-8 MOF molecular sieving material and the high aspect ratio of a nanosheet morphology was probed to induce the *in situ* selective filtration of the undesired chloride ion towards the electrocatalyst surface, namely iridium nanoparticles interdispersed on Vulcan carbon. Cross-sectional analysis revealed a homogeneous dispersion of the nanosheets within the electrocatalytic film. This composite catalyst enabled a ~65 % drop in CER selectivity upon increasing the Zn/Ir molar ratio when evaluated at a disk current density of 3 mA/cm^2 at a chloride ion concentration of 10 mM. Further evaluating the CER selectivity at lower current densities along the disk indicated a near 95 % drop in CER selectivity at 500 mM chloride ion concentration, shown through rotating ring disk electrode experiments. A competitive absorbing mechanism was indicated and the unchanged kinetics of the CER suggests a decrease of the CER current due to an induced diffusional control. The development of a composite architecture enabling the *in operando* filtration of chloride ions seems promising towards producing hydrogen by direct seawater electrolysis.

1. Introduction

Effectuating the production of hydrogen through water electrolysis powered by renewable energy sources requires a near 20 m^3 of water for every ton of hydrogen evolved [1]. The ubiquity of seawater resources would allow the mature hydrogen economy to balance the anthropogenic greenhouse emissions [2,3]. However, relying on seawater desalination facilities to purify the requisite water may jeopardize water resilience within water stressed regions [4]. At present, ameliorating the direct seawater electrolysis requires complementing the hydrogen evolution reaction (HER) at the cathode (Eq. (1)) with an advancement in the conception of material designs that can achieve selectivity for the kinetically encumbered oxygen evolution reaction (OER) at the anode (Eq. (2)).

$$2H^+ + 2e^- \rightarrow H_2 \quad (1)$$

$$2H_2O \rightarrow 4H^+ + O_2 + 4e^- \quad E^0 = 1.23 \text{ V vs. SHE} \quad (2)$$

Indeed, the electrocatalysts producing the highest electrolyzer current densities are most robust under acidic conditions, where the competition between the desired water reactant and parasitic chloride ion becomes especially problematic with the use of seawater. Indeed, the chlorine evolution reaction (CER) leads to the evolution of toxic chlorine gas (Eq. (3)).

$$2Cl^- \rightarrow Cl_2(aq) + 2e^- \quad E^0 = 1.36 \text{ V vs. SHE} \quad (3)$$

The reaction of this evolved gas with water can form hypochlorous acid, which can disproportionate into hypochlorite and contribute to the

* Corresponding author.
E-mail address: cedric.tard@polytechnique.edu (C. Tard).
[1] Presently at Univ Grenoble Alpes, DCM, CNRS, 38000 Grenoble, France.

https://doi.org/10.1016/j.electacta.2025.147664
Received 4 July 2025; Received in revised form 18 October 2025; Accepted 27 October 2025
Available online 28 October 2025

corrosion of the cathode and the degradation of the electrolyzer unit. The chloride ion itself can moreover corrode the anode by replacing the oxygens along the passivated surface and poison the catalysts at both the anode and cathode by affecting their functionality and promoting dissolution [5]. The perilous acidic conditions created by the oxygen evolution at the anode moreover decreases the potential difference between the onset of the OER and the CER, which nonetheless favors the OER thermodynamically, though the CER occurs through a single intermediate and thus will evolve at lower potentials than the OER on oxides.

Thus, a robust electrocatalytic system is required that can selectively catalyze the intensive, four-step reaction of the OER, the mechanism of which remains under contention [6]. Strategies that manipulate the structure of the electrocatalyst by modifying the crystal structure, introducing point defects such as vacancies and substitutions, or modulating the morphology and crystal facet have indicated efficacy towards selecting for the OER or the CER [6]. Indeed, Gong et al. improved the CER selectivity towards 95.7 % by introducing both an Ru dopant and an Sn dopant into a Ru Sn Ti electrode proposed through DFT calculations to promote the CER and inhibit the OER, respectively [7]. However, Astudillo et al. found the proclivity toward CER selectivity to be independent of the Ru content within a single phase $Ru_xMn_{1-x}O_2$ [8] and further reasoned through *in situ* soft X-ray absorption spectroscopy that in presence of chloride ions, Ru *cus* sites can maintain the surface confined -OOH intermediates at potentials negative to the OER onset and enable the OER to evolve, emphasizing that selectivity towards the OER can occur only by leaving the RU *cus* sites free of chloride ions [9].

Thus, a robust electrocatalytic system is required that can selectively catalyze the intensive, four-step reaction of the OER. An iridium electrocatalyst was chosen consisting of 2–4 nm diameter nanoparticles deposited on conductive Vulcan carbon in 10:90 w/w % of iridium and Vulcan carbon and is termed Ir10 in the following work. To prevent the chloride ions diffusion towards the Ir nanoparticle electrocatalysts further requires a mechanism to impede its permeation within the film and prevent the evolution of molecular chlorine. Careful contemplation of the three-dimensional nature of this electrocatalytic system encourages a design in which electrical percolation may be preserved while selectively filtrating the chloride ion to prevent its species transport towards the catalytic nanoparticles. Through exfoliation, Jian et al. developed a two-dimensional (2D) monolayer aluminum tetra-(4-carboxyphenyl) porphyrin framework to create the building blocks for a desalination membrane that achieved a salt rejection of nearly 100 % while maintaining water fluxes reaching 2.2 mol/(m^2•hour·bar) for over 750 h [10]. Patil et al. further applied CoFe-oxyfluorides (CoFeOF) nanosheets anchored on nickel foam towards selective alkaline seawater electrolysis and indicated to impede the species transport of the chloride ion through an electrostatic effect engendered by the highly electronegative oxygen and fluoride ions [11].

Considering the synthetic tunability of MOF materials further facilitates a controlled of porosity and unprecedented surface areas that can achieve ion size exclusion and solute specific chemical interactions [12, 13]. The effective pore size of a 2D ZIF-8 nanosheet is moreover larger than that of the water molecule though smaller than that of many inorganic ions found in seawater and thus could be applied towards water purification technologies [14–16]. Indeed, its effective pore diameter is between the hydrated diameter of the chloride ion (6.64 Å) and the width of the water molecule (2.76 Å), and thus is an attractive candidate to improve the diffusional selectivity and induce a molecular separation of the chloride ion and the desired water reactant to permit the selective OER at the anode [17]. Nanosheet stacks may moreover create longer and more tortuous paths for larger molecules that cannot pass through the pores, while their minimal thicknesses further facilitates the permeation of the smaller molecule [18]. ZIF-8 has been further implemented under the harsh acidic conditions of PEMWE [19,20], having impressive thermal and chemical stabilities [21,22].

In this work, a composite electrocatalyst made of ZIF-8 nanosheets mixed with the Ir10 electrocatalyst is developed and its performance is evaluated with a rotating ring disk electrode under aqueous conditions at various concentrations of NaCl in a perchloric acid supporting electrolyte. We report a near 65 % drop in CER selectivity at a 10 mM NaCl concentration through nanosheet incorporation into the electrocatalytic film using a Zn/Ir molar ratio of 160/1, with an apparent minimal 30 mV increase in potential. Further decreasing the disk current density by evaluating the CER selectivity at lower potentials revealed a near 95 % decrease in CER selectivity at 500 mM chloride ion concentrations. The nanosheets were also found to minimally affect the kinetic mechanism utilized by the iridium nanoparticles to evolve the undesired molecular chlorine: an induced diffusional control mechanism implemented through the integration of the nanosheets within the electrocatalytic film was thus indicated and confirmed.

2. Experiments

The electrocatalyst composite consists of commercial Ir10, which comprises Ir nanoparticles with a diameter of approximately 2 nm, interdispersed on Vulcan Carbon (10 % w/w), and ZIF-8 nanosheets. X-ray photoelectron spectroscopy (XPS) was performed on the Ir10 (Fig. S10) and confirmed the presence of Ir on the carbon support. A transmission electron microscopy picture of Ir10 is shown in Fig. 1a with the acquisition procedure described in the SI. The synthesis of the ZIF-8 nanosheet is based on the work of Jiang et al. [23]. Briefly, zinc nitrate and 2-methylimidazole were mixed at room temperature in water for 24 h. The anisotropic morphology of a nanosheet is proposed to be induced through crystallization in the monoclinic phase [14,15] The ZIF-8 powder is analyzed by X-ray diffraction (Fig. S1) showing that the monoclinic desired phase is obtained as a pure phase with a measured pore diameter of 4.07 Å. The morphology of the resulting nanosheets is characterized through scanning electron microscopy (SEM) as shown in Fig. S2. Pictures reveal a thickness range of 8 nm to 209 nm with highly populated bins that encompass thicknesses of 20 nm and thicknesses of 65 nm. HR-TEM further confirmed the homogeneous size of the nanosheets as shown in Fig. 1b An average nanosheet width of approximately 1000 nm was further observed.

This Ir10 material and ZIF-8 nanosheets are combined in various Zn/Ir molar ratios, ranging from 0/1 (IrZIF0) to 200/1 (IrZIF200) to form an electrocatalytic film. This film is prepared from an ink, which consists of a solution of Nafion (5 % w/w) in a 50/50 w/w mixture of 1-propanol and water, along with additional Vulcan carbon to enhance electrical conductivity. This ink is then drop-casted onto a glassy carbon electrode and allowed to dry, forming a solid electrocatalytic film (see SI for experimental details). In order to probe the architecture of the composite material, scanning electron microscopy (SEM) and energy dispersive X-ray spectroscopy (EDX) are used on the cross-section of the 60/1 Zn/Ir (IrZIF60) electrocatalytic film dropcasted on a Si wafer. The film thickness was determined to be approximately 3 μm, as shown in Fig. 2. Three different regions within the electrocatalytic film are found through EDX elemental mapping, detailed in Figure S3. An SEM image of the first region, shown in Fig. 2a is concentrated with zinc, implying an aggregation of ZIF-8 nanosheets. The second shown in Fig. 2b is devoid of aggregates containing fluorine, an element uniquely found within the Nafion, and zinc, implying that the nanosheets may be interdispersed within the Nafion. Indeed, Wang et al. indicated that the nitrogen atoms on the organic linker within the nanosheets could form an interfacial pair with the sulfate groups within the Nafion, promoting proton conduction within the electrocatalytic film [24]. The third ensemble shown in Fig. 2c consisted of a large quantity of carbon with evidence of Ir as well as Zn. This ensemble indicates that the ZIF-8 nanosheets may be intimately mixed with the Ir10 electrocatalyst, though the relatively low resolution of SEM EDX prevented an evaluation of the element localization at the nanoscale. The elemental composition patterns of these three ensembles obtained the SEM EDS are indicated in the SI. The

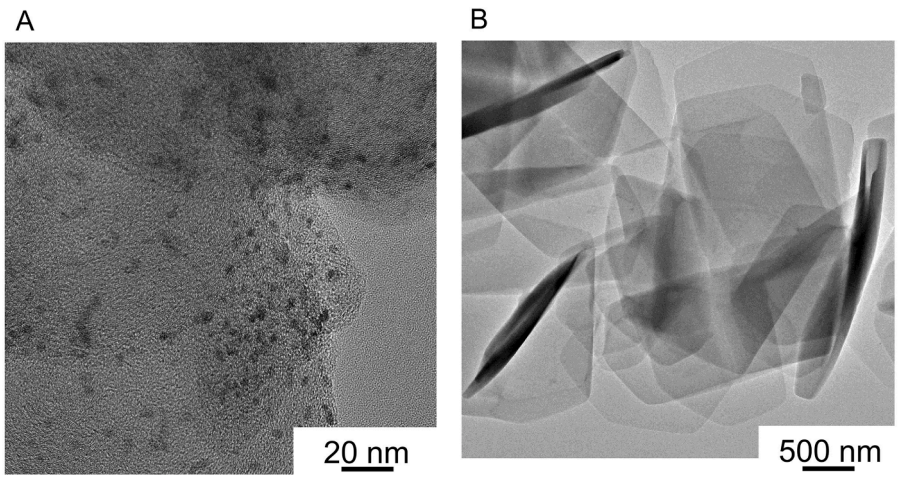

Fig. 1. (a) Transmission electron microscopy image of the Ir10 catalyst with Ir nanoparticles interdispersed in a Vulcan carbon matrix. (b) An HR-TEM image of the ZIF-8 nanosheets.

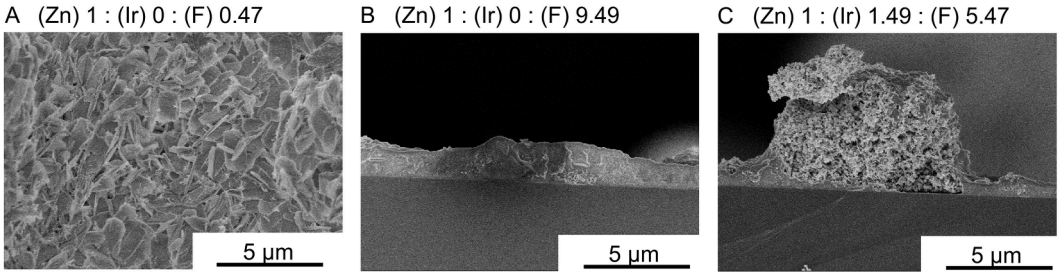

Fig. 2. Magnified SEM images of each elemental ensemble with the Zn:F:Ir weight percent ratio indicated just above.

integration strategy utilized thus appears to promote a rather homogeneous dispersion of the nanosheets amongst the electrocatalytic film constituents.

3. Results and discussion

With reference to Vos et al. [25], an electroanalytical rotating ring disk electrode (RRDE) protocol detailed in the Supporting Information was designed to probe the nanosheet integrated electrocatalytic films under aqueous conditions that thus promote the OER though also the CER through incremental additions of NaCl. The voltammetric sequence under hydrodynamic conditions consisted of electropolishing the platinum ring, conditioning the film, and then performing a linear sweep voltammogram (LSV) at four distinct rotation rates. The ring potential was set to 0.95 V vs. RHE to evade oxygen reduction at the ring [25]. The LSV scan taken at 1600 rpm was used in the CER selectivity computation. Multiplying the ring current (corrected for the film resistance and background current as detailed in the SI) by the collection efficiency (N), the value being obtained from a collection efficiency experiment denoted in the SI, which gives the i_{CER}, and then subtracting that result from the i_{disk} gives the current produced from the OER, the i_{OER},

$$i_{OER} = i_{disk} - i_{CER} = i_{disk} - \left|\frac{i_{ring}}{N}\right| \quad (4)$$

With the i_{CER} and the i_{OER} calculated, the faradaic selectivity for the CER can be derived,

$$E_{CER} = \frac{\frac{i_{CER}}{2}}{\frac{i_{OER}}{4} + \frac{i_{CER}}{2}} \quad (5)$$

The use of sulfuric acid as the acidifying supporting electrolyte may introduce a competitive surface adsorbate that diminishes the effects of the chloride ion on the perceived CER and OER selectivities of the electrocatalytic films [26,27]. Thus, the electroanalytical RRDE protocol was first used to probe the effect of the supporting electrolyte on the CER selectivity. A control electrocatalytic film consisting of Ir10 without incorporation of the nanosheets was subjected to incremental increases in the NaCl concentration. The solutions were acidified with either 0.2 N H_2SO_4 and KNO_3 (pH = 0.8), which was added in the requisite proportion that ensured the ionic strength of each solution was equal, or 0.5 M $HClO_4$ (pH = 0). Ir10 films prepared from the same initial ink trialed with the 0.2 N H_2SO_4/KNO_3 are shown in the red dots of Fig. 3a and Ir10 films from another Ir10 ink trialed in the 0.5 M $HClO_4$ are shown in the blue dots of Fig. 3a with the CER selectivity standard deviation indicated. OER and CER currents are evaluated at the potential which the disk current density arrived at 3 mA/cm^2 during the LSV scan. Indeed, Oener et al. found the perchlorate anion to be weakly absorbing onto their Nafion-ionomer-catalyst composite and minimally affected the impact that the applied bias was shown to have on compensating effect established between the enthalpic activation energies and pre-exponential activation entropies associated with evolving hydrogen on platinum group metal electrode-membrane assemblies [28]. The pre-exponential activation entropy of the reactant ion ($\Delta S = S_t - S_i$) was further indicated to be dependent on the configurational entropy of transition state (S_t), which may be increased by delocalizing the reactant ion over an ordered hydrogen bonding network achieavable in an aqueous supporting electrolyte; increasing the connectivity of the hydrogen bonding network further decreases the entropy of an H_2O reactant (S_i) [28,29]. Thus, introducing the chloride ion within the highly acidic perchloric acid solution may indeed provide a conducive electrostatic environment that can extract the chloride ion from the solution, increasing the configurational entropy of the transition state and thus the rate of the initial desolvation step. The kinetics of the CER then become dominated not by interfacial solvation, though instead by

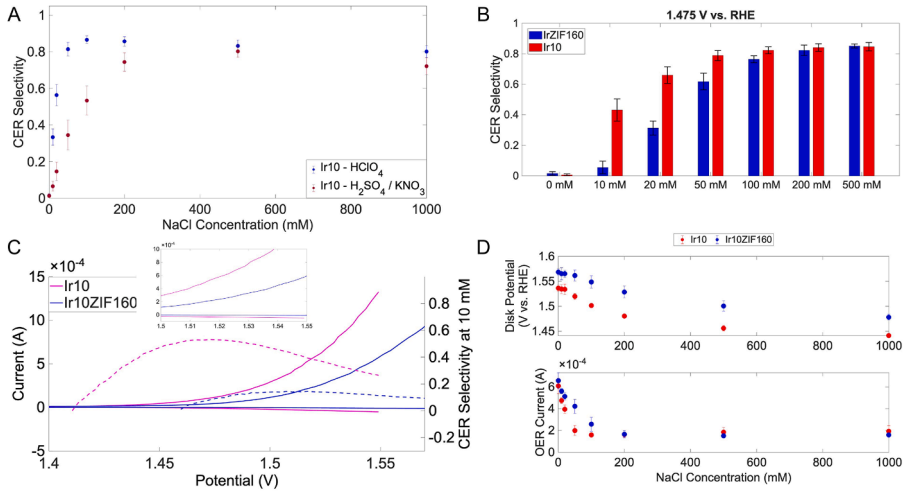

Fig. 3. (a) CER selectivity at 3 mA/cm^2 along the disk at ascending NaCl concentrations in 0.2 N H_2SO_4, 0.5 M KNO_3 (pH = 0.88) or 0.5 M $HClO_4$ (pH = 0) supporting electrolyte. Standard deviations are calculated respectively from five film dropcasted from one ink and four films dropcasted from another ink. (b) Reveals the drop in CER selectivity especially at lower NaCl concentrations through integration of ZIF-8 nanosheets when evaluated at a disk current density of 3 mA/cm^2, potentials vs RHE are indicated just below the respective bar. (c) Displays the LSV curves (solid lines) and the corresponding calculated CER selectivity (dashed lines) for both Ir10 and the Ir10ZIF160 as a function of the potential. (d) Delineates how the potential at which 3 mA/cm^2 is reached at the disk and the OER current are affected by the NaCl concentration.

adiabatic electron transfer and a Butler-Volmer / Marcus-Hush fast kinetic regime [28], evident by the elevated selectivities for the CER as the chloride ion concentration is increased within the perchloric supporting electrolyte in Fig. 3a. To avoid the potential complication of an additional competitive adsorbate, perchloric acid was used as the supporting electrolyte to probe any perceived effect of the ZIF-8 nanosheets on the CER selectivity.

With the electroanalytical RRDE protocol using a 0.5 M concentration of perchloric acid as the supporting electrolyte, electrocatalytic films integrating ZIF-8 nanosheets were probed through LSV at increasing NaCl concentrations. A comparison of the CER selectivity, evaluated at the potential (noted just below the bar graphs) at which the disk current density arrived at 3 mA/cm^2 during the LSV scan, between Ir10 and IrZIF160 is indicated in the bar graphs of Fig. 3b At a fixed Ir10: ZIF-8 ratio, the CER selectivity is increasing with the chlorine concentration. Interestingly, at a fixed chlorine concentration, a decrease in CER selectivity upon increasing the Zn/Ir molar ratio within the electrocatalytic film is observed through NaCl concentrations up to 100 mM. It is apparent that the CER selectivity drops by ~65 % upon increasing the Zn/Ir molar ratio within the MOF incorporated films from 0/1 to 160/1 at 10 mM NaCl as indicated by comparing the dotted curves in Fig. 3c along a potential of 1.53 V. The selectivity towards the CER appears to increase up to about 200 mM as similarly found by Kuznetsova et al., who moreover suggested that this increase occurs until the active sites along the catalytic surface become saturated [30]. Interestingly, the percent drop in CER selectivity through incorporation of the nanosheets is rather consistent up to this concentration referring to Fig. 3b In spite of this observation, a general decrease in the potential required to reach the current density of 3 mA/cm^2 at the disk is observed as can be noted in the top panel of Fig. 3d; as the chloride ion concentration is increased, the potential at which 3 mA/cm^2 along the disk is achieved is observed to decrease. This metric was initially chosen in the evaluation of the CER selectivity of the electrocatalytic films to ensure that the polarization response and resultant potential is controlled by the heterogenous reaction kinetics and is not affected by the gas bubble formation, which can induce ohmic control of the electrode potential and evolve the exponential J-E relationship into a linear J-E relationship, obscuring the evaluation of the kinetic response to an applied potential [31,32]. Moreover, defining a discrete current density to evaluate the CER selectivities of the electrocatalytic films enabled the variability amongst the films to be calculated. The low variability observed suggests that the stability of the nanosheet-integrated films was maintained throughout the analysis. Additionally, it indicates that the electrochemical surface area of the Ir10 electrocatalyst remained consistent across the tested films. However, imposing this limitation affects the evaluation of the nanosheet performance at elevated chloride ion concentrations by means of a CER selectivity analysis. The CER selectivity is indeed being evaluated at a lower potential, a potential which may indeed be lower than the driving force required to promote the generation of the OER intermediates. This decrease in potential thus disfavors the OER by becoming insufficient to promote its catalysis [30]. As is indeed shown in Fig. 3d, upon increasing the NaCl concentration, the contributing OER current measured as the disk current achieves 3 mA/cm^2 begins to decrease, presumably because the potential at which the disk current density achieves 3 mA/cm^2 lessens. Thus, evaluation of the performance of the ZIF-8 nanosheets through calculation of the CER selectivity at a fixed current density of 3 mA/cm^2 may be convoluted by the decrease in OER current that become appreciable as the chloride concentration increases and the potential at that current density along the disk decreases; indeed, a denominator factor is diminishing.

Moreover, the group of Krtil found that no oxygen could be detected at chloride concentrations above 50 mM in 0.1 M $HClO_4$ supporting electrolyte [30]. Though nanosheet incorporation into an electrocatalytic film appears to enable the OER up to NaCl concentrations of at least 100 mM at a disk current density of 3 mA/cm^2 as shown in Fig. 3d These nanosheets may indeed have continued performance at elevated NaCl concentrations. However, the decreasing potential apparent upon increasing the chloride ion concentration convolutes the analysis, indicating the imperativeness of a robust *in situ* filtration mechanism that can mitigate any slightest available transport path for the approach of the chloride ion towards the electrocatalyst [33].

Deciphering the effect that the potential may indeed have on the CER selectivity may become apparent by plotting the CER selectivity as a function of the potential shown for the first trial of the Ir10 and the IrZIF160 in Fig. 4a. The potential is known to dictate the electron transfer rate constant and thus the activation barrier for the catalysis [34,35]. Decreasing the potential applied, the driving force for the OER and CER electrochemical reactions, decreases the current density at which the CER selectivity is evaluated and reveals how the intrinsic rate of the CER may be affected by the presence of the ZIF-8 nanosheets.

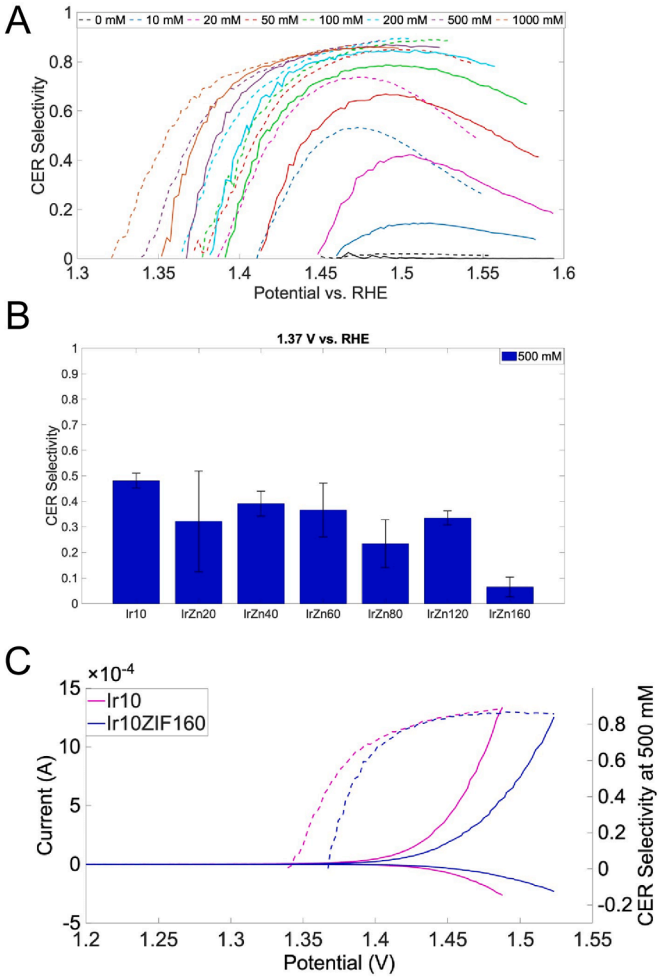

Fig. 4. (a) Plot of the CER selectivity vs. potential from a trial of the Ir10 electrocatalytic film shown in dashed lines and the IrZIF160 electrocatalytic film shown in solid lines at NaCl concentrations ranging from 0 mM to 1000 mM. (b) Evaluation of the CER selectivity of electrocatalytic films with different Zn/Ir molar ratios at a potential of 1.37 V vs. RHE.

Indeed, it can be seen at a potential of 1.37 V vs. RHE, just above the thermodynamically reversible voltage for the CER, that a 160/1 ZIF/Ir molar ratio decreases the CER selectivity by a near 95 % at a concentration of 500 mM NaCl, as shown by comparing the red and blue dotted lines of Fig. 4b and the bar graphs of Fig. 4c. Thus, the nanosheets do appear to effectively arrest the CER at chloride ion concentrations similar to that of seawater. The nanosheets may indeed be effective at arresting the CER at a higher applied bias and greater currents, though Öner et al. indicated that increasing the applied bias may decrease the configurational entropy of the water reagent by increasing the connectivity of the hydrogen bonding network, decreasing its pre-exponential activation entropy, and decreasing the catalytic rate of the OER at the surface of the iridium nanoparticles [28]. Indeed, this effect may arise from the inception of capacitive charging, which below a bias of 200 mV, was shown to induce entropic changes in the water network, changing preexponential factors rather than activation enthalpies [36]. Moreover, this effect increases the configurational entropy of the transition state for the chloride ion and desolvation rate, promoting adiabatic electron transfers and the fast kinetic regime [28].

Moreover, the applied potential measured at a constant current density along the disk seemed only slightly to vary with the Zn/Ir molar ratio. Only a ~30 mV difference between the Ir10 and the ZIFintfilm160 is perceived, as shown in Fig. 5a. Furthermore, knowing that the resultant current density at the disk is a summation of the achievable

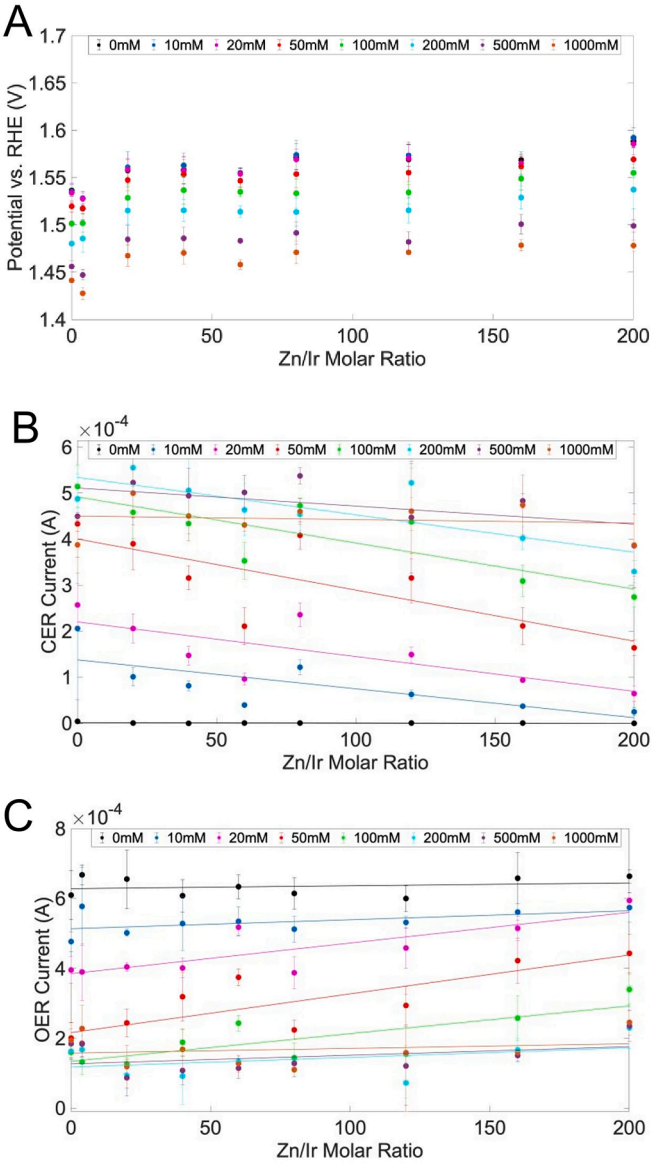

Fig. 5. (a) Potential measured when a current density of 3 mA/cm^2 is reached at the disk as a function of the Zn/Ir molar ratio within the film. (b) Deconvoluted CER current measured at the disk at a total disk current density of 3 mA/cm^2 as a function of the Zn/Ir molar ratio within the film. (c) Deconvoluted OER current measured at the disk at a total disk current density of 3 mA/cm^2 as a function of the Zn/Ir molar ratio within the film.

OER current and the CER current, deducible through the presence of the ring set to a selective potential at which the current from the CRR can be measured, the OER and CER currents may be evaluated, here at a current density of 3mA/cm^2 and plotted as a function of Zn/Ir molar ratio in the film as shown in Fig. 5b and 5c, the corresponding potentials can be deduced by referring to Fig. 5a. These figures indicate both a slight increase in OER current at increasing Zn/Ir ratios with a simultaneous decrease in CER current with an increasing Zn/Ir ratios. The ZIF- phase thus doesn't appear to decrease the water permeability even at heightened nanosheet quantities. Moreover, increasing the quantity of this molecular sieving material with this characterized pore aperture appears to selectively impede the CER current and promote the OER current, suggesting that catalytic active sites that can bind the water substrate and the intermediates of the OER are being liberated. This phenomenon supports the work of Koper et al. who indicated that the water substrate for OER and the chloride ion substrate of the CER

compete for the catalytic active sites along the electrocatalytic surface [26]. Achieving a heterogeneous electrocatalytic system design with selective facets and additional point defects that modulate these active sites to selectively catalyze the OER over the CER has been discussed [6]. This in-situ filtration strategy discussed herein indicates that increased nanosheet quantities within the electrocatalytic film may provide another means of hindering the CER current while promoting the OER, presumably by impeding the substrate diffusion for the CER within the film towards the active sites.

The current measured at the disk (and the ring) of a modified electrode is however governed by a number of processes including the electron transfer kinetics at the catalytic active sites, the movement of electrons between the electrode and those interdispersed active sites, and the rates of substrate mass transport within the film and within the surrounding solution [37]. The presence of Vulcan carbon within the film is assumed to create a fast conducting film, thus determining whether the CER current is under diffusional control may be conducted by verifying that the kinetic current is indeed consistent both with and without the nanosheets, which may be conducted through rotating ring disk voltammetry with a Koutecky-Levich analysis [38]. However, the diffusion-limiting plateau current was never reached in the present study. Practically, significant bubble generation limited the ability to achieve current densities higher than 5–10 mA/cm^2 before detachment of the film from the working electrode surface. Moreover, higher current densities would increase the generation of gas bubbles that may enhance the ohmic drop between the working and reference electrode and deceive the interpretation of the limiting current if not properly compensated [39]. Furthermore, cyclic voltammetry analysis of the electrocatalytic film to determine if the current is under kinetic control is limited when the substrate is the reagent and impractical when the thickness of the film cannot be varied to render a foot-in-the-wave analysis [40].

The degree of kinetic control of the CER current within the electrocatalytic film, and thus the determination of the kinetically or diffusionally induced mechanism through which the nanosheets may selectively impede the CER current, may become apparent through the evaluation of the reaction order of the kinetic mechanism as well as the Tafel slope of the CER occurring at the iridium nanoparticles within the electrocatalytic film. Indeed, as previously discussed, the CER appears to be following a Butler-Volmer/Marcus-Hush fast kinetic regime within these conditions [28]. Following the work of Tilak and Conway [41], the reaction order (Eq. (6)) and Tafel slope (Eq. (7)) may be defined,

$$R = \frac{\partial \ln (J)}{\partial \ln [Cl^-]} \tag{6}$$

$$b = \frac{\partial \eta}{\partial \log(j)} \tag{7}$$

The evolution of the CER on iridium is further thought to occur through a sequence of intermediates chemisorbed onto the catalytic surface. This process is governed by rate-limiting steps proposed by Heyrovsky, Krishtalik, and Tafel [6]. Consequently, the evolved CER current is dependent not only on the concentration of the substrate though also on the coverage of the chemisorbed intermediate(s) defining the rate limiting step on that surface (θ). This coverage is expressed as a fraction between zero and one, which may be related to the substrate concentration through an adsorption isotherm. The assumption that the Langmuir isotherm applies,

$$\theta = \frac{K_{Cl}[Cl^-]e^{f\eta}}{K_{Cl}[Cl^-]e^{f\eta} + 1} \tag{8}$$

enables an initial assessment of the degree of dependence that the chemisorbed intermediates of the rate limiting step invoke on the reaction velocity [26]. The reaction order and Tafel slope of the electrocatalytic films with and without the presence of the nanosheets was evaluated through the plots shown in Fig. 6. Low Tafel slopes between 55 – 82 mV/decade and a reaction order between 0 and 1 were obtained for electrocatalytic films both with and without the presence of the nanosheets, displayed in Table S1. This occurrence implies that the transfer of the first electron is rather reversible, and it is the transfer of the second electron or a subsequent chemical reaction that represents the rate limiting step [42]. Indeed, the low reaction order rejects the slow recombination mechanism characteristic of the Heyrovsky mechanism and implies that the mechanism follows the proposal of Krishtalik, which is in line with previous studies [26]. The consistency of the Tafel slopes in Fig. 6b for the electrocatalytic films both with and without the nanosheets could be a further indication of the minimal effect that the nanosheets have on the resistivity of the film [43]. Furthermore a graph representing the potential measured at the current density of 3 mA/cm^2 against the natural logarithm of each chloride ion concentration probed, is shown in Fig. S8. This graph reveals similar slopes for the electrocatalytic films both with and without the presence of the nanosheets. There appears to be a change in the slopes as the chloride ion concentration decreases below 50 mM, and this change is consistent in all cases. This indicates that the product of the reaction order and Tafel slope remains unaffected by the presence of the nanosheets. The change in slopes might be due to a change in the transfer coefficient, as suggested in previous studies [41,42].

The kinetic mechanism remains consistent both with and without the presence of nanosheets integrated within the film. This suggests that the incorporation of nanosheets does not induce kinetic control but rather a diffusional control of the CER current. Further evaluation of the evolved current at a potential within the mass transfer controlled region was conducted for an Ir10ZIF40 film (1.6 V vs. RHE), as shown in Fig. S8. A comparison with simulated Cottrell conditions under semi-infinite spherical diffusion, assuming a chloride ion diffusion coefficient of 1.77×10^{-5} cm^2/sec, is additionally plotted. The observed inverse $t^{1/2}$ dependence with respect to the evolved current clearly indicates a depletion of the electroactive species near the electrode surface and an induced diffusional control [37]. Indeed, investigations of other processes that may limit the evolved CER current, such as convective diffusion within the surrounding solution, were attempted by conducting the electroanalytical RRDE protocol at different rotation rates. The LSV curves of the control Ir10 film, probed at different concentrations of NaCl with rotation rates of 500 rpm, 1000 rpm, 1600 rpm, and 2000 rpm, are shown in Fig. S9, and appear to be independent of the rotation rate. Thus, the evolved current of the system does not appear to be kinetically limited.

Another kinetic component that must be considered is the crossing of the chloride ion reagent between the solution and the film. This penetration rate may be characterized by assuming a pinhole distribution of aperture widths equivalent to that of the nanosheet located at an equivalent distance from one another [44]. In addition, the high aspect ratio of the nanosheets enables a morphological stacking of the material that provides an additional means of sieving; longer and more tortuous paths are created for the larger molecule that cannot pass through the pores. Thus, augmenting the pinhole distribution model with an additional tortuosity parameter may elucidate the limitation that the reagent film penetration rate may impose on the CER current. The mechanism that may indeed be rendering the evidenced diffusional control may be determined. Further development of a nanosheet integration strategy that enables control of the resulting electrocatalytic film architecture may enable these sieving mechanisms to be trialed, enhancing the decryption of the degree of diffusional impediment that each mechanism may impose within the electrocatalytic film and enable a design that accentuates the desired sieving effect.

4. Conclusions

By means of an incorporation of monoclinic ZIF-8 nanosheets into electrocatalytic films composed of iridium nanoparticles interdispersed

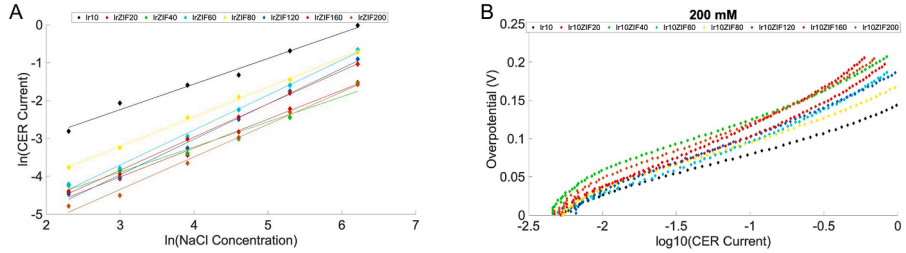

Fig. 6. (a) log of the calculated CER current against the log of the NaCl concentration for both Ir10 and varying Zn/Ir ratios of nanosheets at a potential of 1.48 V for the determination of the Reaction Order of the CER kinetic mechanism. (b) Tafel plot for both Ir10 and varying Zn/Ir ratios of nanosheets at an NaCl concentration of 200 mM.

on Vulcan carbon, the CER selectivity during electrocatalysis of simulated seawater water dropped by 65 % at low chloride ion concentrations when evaluated at a disk current density of 3 mA/cm^2. Further elucidation of the current density metric was achieved by plotting the CER selectivity as a function of the potential. A dramatic drop of 95 % in CER selectivity became apparent with the utilization of an electrocatalytic film consisting of a 160/1 Zn/Ir molar ratio when evaluated at 1.37 V vs. RHE. Thus, the implementation of ZIF-8 nanosheets into an electrocatalytic film appears promising. The electrocatalytic activity of the iridium nanocluster catalysts was minimally affected by the presence of the nanosheets, indicated by the small increase in the potential at which a current density of 3 mA/cm^2 was reached at the disk. Deconvoluting that current density at the disk into the respective OER and CER current contributions revealed a decrease in the CER current and an increase in the OER current upon increasing the Zn/Ir molar ratio. This indicates clearly a competitive adsorbing mechanism. The presence of nanosheets at the electrode doesn't modify the kinetic mechanism of the CER, confirming the diffusional control of the CER current. Development of a nanosheet integration strategy that enables control of the resulting electrocatalytic film architecture may enable the sieving mechanism to be elucidated and further optimized to promote the substantial decrease in CER selectivity at elevated current densities under 500 mM chloride ion concentrations. The efficacious effect on selective evolution of the OER in the presence of the nanosheets indicates that a venture into the two-dimensional realm of novel materials may divulge a potent inception towards the realization of electrolysis with unpurified water sources.

Abbreviations

HER, Hydrogen Evolution Reaction; OER, Oxygen Evolution Reaction; CER, Chlorine Evolution Reaction; 2D, Two-Dimensional; MOF, Metal-Organic Framework; PEMWE, Proton Exchange Membrane Water Electrolysers; ZIF-8, Zeolite Imidazole Framework – 8; Ir10, Iridium electrocatalytic film; HR-TEM, High-Resolution Transmission Electron Microscopy; EDX, Energy Dispersive X-Ray Spectroscopy; RRDE, Rotating Ring Disk Electrode; LSV, Linear Scanning Voltammetry; RPM, rotations per minute.

Funding sources

This work has been carried out at the Energy4Climate Interdisciplinary Center (E4C) of IP Paris and Ecole des Ponts ParisTech, which is in part supported by 3rd Programme d'Investissements d'Avenir [ANR-18-EUR-0006–02], and by the Foundation of Ecole polytechnique with the private sponsor Fonds Ifker pour le Climat, financed by Stéphane and Agnès Ifker.

CRediT authorship contribution statement

Catherine Harvey: Writing – original draft, Methodology, Formal analysis, Data curation. **Simon Delacroix:** Writing – review & editing, Supervision, Methodology, Formal analysis, Conceptualization. **Clément Marchat:** Writing – review & editing, Formal analysis. **Thierry Gacoin:** Writing – review & editing, Supervision, Methodology, Formal analysis, Conceptualization. **Cédric Tard:** Writing – review & editing, Supervision, Project administration, Methodology, Investigation, Funding acquisition, Data curation, Conceptualization.

Declaration of competing interest

The authors declare that they have no known competing financial interests or personal relationships that could have appeared to influence the work reported in this paper.

Acknowledgements

The authors most sincerely thank Professor Cyrille Costentin for his insightful thoughts and discussions. We thank the CIMEX team (Centre Interdisciplinaire de Microscopie Electronique en transmission de l'Ecole Polytechnique) for the help provided in acquiring and interpreting TEM, SEM and EDX data. Philippe Decorse is gratefully acknowledged for conducting XPS experiments, and we acknowledge the ITODYS XPS-UPS facility (Université Paris Cité, CNRS UMR 7086, Paris, France).

Supplementary materials

Supplementary material associated with this article can be found, in the online version, at doi:10.1016/j.electacta.2025.147664.

Data availability

Data will be made available on request.

References

[1] D. Olaitan, M. Bertagni, A. Porporato, The water footprint of hydrogen production, Sci. Total. Environ. 927 (2024) 172384, https://doi.org/10.1016/j.scitotenv.2024.172384.
[2] J.O.M. Bockris, A hydrogen economy, Science (1979) 176 (4041) (1972) 1323, https://doi.org/10.1126/science.176.4041.1323.
[3] Council, H.; Company, M. *Hydrogen Insights 2022: an updated perspective on hydrogen market development and actions required to unlock hydrogen at scale.*; 2022.
[4] P. Woods, H. Bustamante, K.-F. Aguey-Zinsou, The hydrogen economy - where is the water? Energy Nexus. 7 (2022) 100123 https://doi.org/10.1016/j.nexus.2022.100123.
[5] F. Zhang, L. Yu, L. Wu, D. Luo, Z. Ren, Rational design of oxygen evolution reaction catalysts for seawater electrolysis, Trends. Chem. 3 (6) (2021) 485–498, https://doi.org/10.1016/j.trechm.2021.03.003.
[6] C. Harvey, S. Delacroix, C. Tard, Unraveling the competition between the oxygen and chlorine evolution reactions in seawater electrolysis: enhancing selectivity for green hydrogen production, Electrochim. Acta 497 (2024) 144534, https://doi.org/10.1016/j.electacta.2024.144534.
[7] H. Gong, B. Zhu, D. Zhang, T. Liu, P. Kuang, J. Yu, Ru dopant induced high selectivity and stability of ternary RuSnTi electrode toward chlorine evolution reaction, Appl. Cat. B 349 (2024) 123892, https://doi.org/10.1016/j.apcatb.2024.123892.

[8] C. Astudillo, K.M. Macounová, R. Nebel, J. Plšek, P. Krtil, Selectivity of Mn rich RuMnO phases in parallel oxygen and chlorine evolution, Electrochim. Acta 492 (2024) 144346, https://doi.org/10.1016/j.electacta.2024.144346.
[9] C. Astudillo, K. Sakata, R. Nebel, K. Minhová Macounová, K. Amemiya, P. Krtil, Mechanistic aspects of the selectivity of RuO_2 and Ru–Mn–O catalysts in parallel chlorine and oxygen evolutions reactions, ACS Electrochem. 1 (2025) 1314–1326, https://doi.org/10.1021/acselectrochem.5c00033.
[10] M. Jian, R. Qiu, Y. Xia, J. Lu, Y. Chen, Q. Gu, R. Liu, C. Hu, J. Qu, H. Wang, et al., Ultrathin water-stable metal-organic framework membranes for ion separation, Sci. Adv. 6 (23) (2020) eaay3998, https://doi.org/10.1126/sciadv.aay3998.
[11] S.A. Patil, A.C. Khot, V.D. Chavan, I. Rabani, D.-K. Kim, J. Jung, H. Im, N. K. Shrestha, Electrostatically robust CoFeOF nanosheet against chloride for green-H_2 production in alkaline seawater electrolysis, Chem. Eng. J. 480 (2024) 146545, https://doi.org/10.1016/j.cej.2023.146545.
[12] S. Dutta, R.F. de Luis, J. Goscianska, A. Demessence, R. Ettlinger, S. Wuttke, Metal–organic frameworks for water desalination, Adv. Funct. Mater. 34 (2023) 2304790, https://doi.org/10.1002/adfm.202304790.
[13] J.R. Werber, C.O. Osuji, M. Elimelech, Materials for next-generation desalination and water purification membranes, Nat. Rev. Mater. 1 (5) (2016) 16018, https://doi.org/10.1038/natrevmats.2016.18.
[14] Y. Song, M. He, J. Zhao, W. Jin, Structural manipulation of ZIF-8-based membranes for high-efficiency molecular separation, Sep. Purif. Technol. 270 (2021) 118722, https://doi.org/10.1016/j.seppur.2021.118722.
[15] X.-P. Wang, J. Hou, F.-S. Chen, X.-M. Meng, In-situ growth of metal-organic framework film on a polydopamine-modified flexible substrate for antibacterial and forward osmosis membranes, Sep. Purif. Technol. 236 (2020) 116239, https://doi.org/10.1016/j.seppur.2019.116239.
[16] Z. Hu, Y. Chen, J. Jiang, Zeolitic imidazolate framework-8 as a reverse osmosis membrane for water desalination: insight from molecular simulation, J. Chem. Phys. 134 (13) (2011) 134705, https://doi.org/10.1063/1.3573902.
[17] W.J. Koros, C. Zhang, Materials for next-generation molecularly selective synthetic membranes, Nat. Mater. 16 (3) (2017) 289–297, https://doi.org/10.1038/nmat4805.
[18] W. Kim, S. Nair, Membranes from nanoporous 1D and 2D materials: a review of opportunities, developments, and challenges, Chem. Eng. Sci. 104 (2013) 908–924, https://doi.org/10.1016/j.ces.2013.09.047.
[19] L. Hu, R. Xiao, D. Du, C. Zhu, Y. Lin, Metal-organic framework-based electrocatalysts for acidic oxygen evolution reaction, Trends. Chem. 5 (4) (2023) 324–335, https://doi.org/10.1016/j.trechm.2023.02.001.
[20] L. Qiu, G. Zheng, Y. He, L. Lei, X. Zhang, Ultra-small Sn-RuO_2 nanoparticles supported on N-doped carbon polyhedra for highly active and durable oxygen evolution reaction in acidic media, J. Chem. Eng. 409 (2021) 128155, https://doi.org/10.1016/j.cej.2020.128155.
[21] K.S. Park, Z. Ni, A.P. Côté, J.Y. Choi, R. Huang, F.J. Uribe-Romo, H.K. Chae, M. O'Keeffe, O.M. Yaghi, Exceptional chemical and thermal stability of zeolitic imidazolate frameworks, Proc. Natl. Acad. Sci 103 (27) (2006) 10186–10191, https://doi.org/10.1073/pnas.0602439103.
[22] Y. Pan, Y. Liu, G. Zeng, L. Zhao, Z. Lai, Rapid synthesis of zeolitic imidazolate framework-8 (ZIF-8) nanocrystals in an aqueous system, Chem. Commun. 47 (7) (2011) 2071–2073, https://doi.org/10.1039/C0CC05002D.
[23] Y. Jiang, H. Liu, X. Tan, L. Guo, J. Zhang, S. Liu, Y. Guo, J. Zhang, H. Wang, W. Chu, Monoclinic ZIF-8 nanosheet-derived 2D carbon nanosheets as sulfur immobilizer for high-performance lithium sulfur batteries, ACS. Appl. Mater. Interfaces. 9 (30) (2017) 25239–25249, https://doi.org/10.1021/acsami.7b04432.
[24] L. Wang, N. Deng, G. Wang, J. Ju, M. Wang, B. Cheng, W. Kang, Construction of interpenetrating transport channels and compatible interfaces via a zeolitic imidazolate framework "bridge" for nanofibrous hybrid PEMs with enhanced proton conduction and methanol resistance, ACS. Sustain. Chem. Eng. 8 (34) (2020) 12976–12989, https://doi.org/10.1021/acssuschemeng.0c03833.
[25] J.G. Vos, M.T.M. Koper, Measurement of competition between oxygen evolution and chlorine evolution using rotating ring-disk electrode voltammetry, J. Electroanal. Chem. 819 (2018) 260–268, https://doi.org/10.1016/j.jelechem.2017.10.058.
[26] J.G. Vos, A. Venugopal, W.A. Smith, M.T.M. Koper, Competition and selectivity during parallel evolution of bromine, chlorine and oxygen on IrO_x electrodes, J. Catal. 389 (2020) 99–110, https://doi.org/10.1016/j.jcat.2020.05.024.
[27] J.A. Arminio-Ravelo, A.W. Jensen, K.D. Jensen, J. Quinson, M. Escudero-Escribano, Electrolyte effects on the electrocatalytic performance of iridium-based nanoparticles for oxygen evolution in rotating disc electrodes, Chemphyschem. 20 (22) (2019) 2956–2963, https://doi.org/10.1002/cphc.201900902.
[28] J.M. Gisbert-González, C.G. Rodellar, J. Druce, E. Ortega, B.R. Cuenya, S.Z. Oener, Bias dependence of the transition state of the hydrogen evolution reaction, J. Am. Chem. Soc. 147 (6) (2025) 5472–5485, https://doi.org/10.1021/jacs.4c18638.
[29] F. Sarabia, C. Gomez Rodellar, B. Roldan Cuenya, S.Z. Oener, Exploring dynamic solvation kinetics at electrocatalyst surfaces, Nat. Commun. 15 (1) (2024) 8204, https://doi.org/10.1038/s41467-024-52499-9.
[30] E. Kuznetsova, V. Petrykin, S. Sunde, P. Krtil, Selectivity of nanocrystalline IrO_2-based catalysts in parallel chlorine and oxygen evolution, Electrocatalysis 6 (2) (2015) 198–210, https://doi.org/10.1007/s12678-014-0233-y.
[31] P.A. Kempler, R.H. Coridan, L. Luo, Gas evolution in water electrolysis, Chem. Rev. 124 (19) (2024) 10964–11007, https://doi.org/10.1021/acs.chemrev.4c00211.
[32] C. Vogt, B.M. Weckhuysen, The concept of active site in heterogeneous catalysis, Nat. Rev. Chem. 6 (2022) 89–111, https://doi.org/10.1038/s41570-021-00340-y.
[33] D.L. Gin, R.D. Noble, Designing the next generation of chemical separation membranes, Science (1979) 332 (6030) (2011) 674–676, https://doi.org/10.1126/science.1203771.
[34] V. Fourmond, P.-A. Jacques, M. Fontecave, V. Artero, H_2 evolution and molecular electrocatalysts: determination of overpotentials and effect of homoconjugation, Inorg. Chem. 49 (22) (2010) 10338–10347, https://doi.org/10.1021/ic101187v.
[35] R. Parsons, The rate of electrolytic hydrogen evolution and the heat of adsorption of hydrogen, Trans. Faraday Soc. 54 (1958) 1053–1063, https://doi.org/10.1039/TF9585401053.
[36] C.G. Rodellar, J.M. Gisbert-Gonzalez, F. Sarabia, B. Roldan Cuenya, S.Z. Oener, Ion solvation kinetics in bipolar membranes and at electrolyte–metal interfaces, Nat. Energy 9 (5) (2024) 548–558, https://doi.org/10.1038/s41560-024-01484-z.
[37] A.J.F. Bard, R. Larry, Henry S White, Electrochemical Methods: Fundamentals and Applications, John Wiley & Sons, 2022.
[38] W. Chen, H.-W. Cui, L.-W. Liao, Y.-J. Xu, J. Cai, Y.-X. Chen, Challenges in unravelling the intrinsic kinetics of gas reactions at rotating disk electrodes by Koutecky–Levich equation, J. Phys. Chem. C 127 (33) (2023) 16235–16248, https://doi.org/10.1021/acs.jpcc.3c02677.
[39] D. van der Vliet, D.S. Strmcnik, C. Wang, V.R. Stamenkovic, N.M. Markovic, M.T. M. Koper, On the importance of correcting for the uncompensated ohmic resistance in model experiments of the oxygen reduction reaction, J. Electroanal. Chem. 647 (1) (2010) 29–34, https://doi.org/10.1016/j.jelechem.2010.05.016.
[40] C. Costentin, J.-M. Saveant, Cyclic voltammetry analysis of electrocatalytic films, J. Phys. Chem. C 119 (22) (2015) 12174–12182, https://doi.org/10.1021/acs.jpcc.5b02376.
[41] B.V. Tilak, B.E. Conway, Analytical relations between reaction order and Tafel slope derivatives for electrocatalytic reactions involving chemisorbed intermediates, Electrochim. Acta 37 (1992) 51–61, https://doi.org/10.1016/0013-4686(92)80011-A.
[42] L.I. Krishtalik, Kinetics and mechanism of anodic chlorine and oxygen evolution reactions on transition metal oxide electrodes, Electrochim. Acta 26 (3) (1981) 329–337, https://doi.org/10.1016/0013-4686(81)85019-0.
[43] D.Y. Chung, S. Park, P.P. Lopes, V.R. Stamenkovic, Y.-E. Sung, N.M. Markovic, D. Strmcnik, Electrokinetic analysis of poorly conductive electrocatalytic materials, ACS. Catal. 10 (9) (2020) 4990–4996, https://doi.org/10.1021/acscatal.0c00960.
[44] J.M. Savéant, C. Costentin, Elements of Molecular and Biomolecular Electrochemistry, John Wiley and Sons, Inc., 2019, p. 119.